Journal of Environmental Chemical Engineering 11 (2023) 110756

Contents lists available at ScienceDirect

Journal of Environmental Chemical Engineering

journal homepage: www.elsevier.com/locate/jece

A comprehensive approach to simulation of cartridge filtration using CFD

Arsalan Afkhami [a], Alan Brown [a], Lyda P. Sabogal-Paz [b], Dorian Dixon [a], Nigel G. Ternan [c], Patrick S.M. Dunlop [a,*]

[a] School of Engineering, Ulster University, York Street, Belfast, BT15 1AP, UK
[b] São Carlos School of Engineering, University of São Paulo, São Paulo, Brazil
[c] School of Biomedical Sciences, Ulster University, Cromore Road, Coleraine, BT52 1SA, UK

ARTICLE INFO

Editor: Despo Kassinos

Keywords:
Filtration
Particle deposition
CFD
Simulation
Porous media
Household water treatment

ABSTRACT

Household water treatment (HWT) systems are widely used for the provision of potable water in many countries with their low-cost key to attaining universal and equitable access to safe and affordable drinking water, Sustainable Development Goal 6.1. Removal of suspended particles (turbidity) from water sources via cartridge filters is often the first step of a HWT system, with the primary treatment increasing the efficiency of a subsequent disinfection step.

Whilst the performance of cartridge filters (removal efficiency and pressure drop) can be determined experimentally in long experiments with high volumes of water, numerical simulation adds fundamental insight to the influence of fluid dynamics on particle deposition and vice versa. In this study, a novel computational fluid dynamic (CFD) model was developed to simulate the fundamental mechanisms underpinning the removal of particles within the widely used 10 in. cartridge filter, informed by and complemented with laboratory validation. The Eulerian approach was used to simulate fluid flow with the Lagrangian approach adopted for particle tracking. Rosin-Rammler distribution was implemented with respect to the particle size distribution of the diatomaceous earth particles used in the experiments. Given particles were non-spherical (disk shape), Wadell's sphericity was included to account for the effect of particle shape on drag force. A porous domain was implemented to simulate the filter element through addition of a source term to the momentum equations, with the likelihood of particle deposition, detachment and rebound also considered.

Laboratory based validation studies confirmed the novel CFD model to accurately model removal of turbidity and predict the pressure drop across the filter with Root Mean Square Percentage Error (RMSPE) of less than 3%. The simulated location of particle deposition on the filter elements closely matched images taken at several stages during filtration experiments with the model aiding understanding of pattern of particle removal along and within the porous filter structure. This novel and comprehensive modelling methodology can be utilized to simulate the filtration process at the macro-scale, permitting evaluation of new filter designs and materials for advanced filtration systems; ultimately improving HWT system performance and reducing costs to users.

1. Introduction

Over one billion people lack access to safe drinking water [1], with waterborne diseases caused by consumption of unsafe drinking water a major health burden in developing countries [2]. Where the provision of safe and reliable centralised water treatment is not available, effective household water treatment (HWT) and safe storage has been shown to significantly reduce incidence of waterborne disease [3]. The user friendly, low-cost, low-maintenance processes enable access to safe drinking water in keeping with the aims of SDG 6 to provide equitable access to safe and affordable drinking water to all [4].

Cartridge filters are used in point-of-use/household water treatment systems to remove suspended particles. Whilst available at low cost, cartridges filter can quickly block with particles when processing high turbidity effluents, or with extended use. Users often bypass the filters if new consumable parts are not available. The design of cartridge filters could be improved with a greater understanding of how and where particles build up on the surface, resulting in poor filtration performance. To aid with physical experiments in the lab, a modelling

* Corresponding author.
E-mail addresses: afkhami-a@ulster.ac.uk (A. Afkhami), a.brown@ulster.ac.uk (A. Brown), lysaboga@sc.usp.br (L.P. Sabogal-Paz), d.dixon@ulster.ac.uk (D. Dixon), ng.ternan@ulster.ac.uk (N.G. Ternan), psm.dunlop@ulster.ac.uk (P.S.M. Dunlop).

https://doi.org/10.1016/j.jece.2023.110756
Received 12 April 2023; Received in revised form 4 July 2023; Accepted 11 August 2023
Available online 19 August 2023

Nomenclature

Greek symbols

α	permeability, m^2.
η	transport efficiency, –.
γ	porosity coefficient, –.
μ	viscosity, kg/(m s).
Ψ	Wadell's sphericity, –.
ρ	density, kg/m^3.
σ	specific deposition, kg/m.
ε	bed porosity, –.

Other symbols

H	Hamaker constant, J.
τ_r	relaxation time, s.
A_S	porosity function, –.
C	concentration, kg/m^3.
C_2	inertial resistance factor, –.
C_p	coordinates of mesh cell where particle, p, is located.
C_D	drag coefficient, –.
C_L	time scale constant, –.
d	diameter, m.
d_f	fibre diameter, m.
D_L	diffusion coefficient, m^2/s.
F	net force acting on an depositing particle in a filter along the tangential direction, N.
F_f	friction force against particle sliding, N.
F_s	hydrodynamic drag force on a particle, N.
k_B	Boltzmann constant, 1.381×10^{-23} J/K.
k_f	coefficient of sliding friction, –.
k_f'	proportionality constant, m.
m_p	particle mass, kg.
N	number, –.
n	spread parameter, –.
n_{fibre}	approximate number of fibres in 1 mm.
R_p	particle distance from the outer surface of the filter, m.
Re	Reynolds number, –.
S	momentum source term.
S	specific surface area, m^{-1}.
T	absolute temperature, K.
T_L	fluid Lagrangian integral time, –.
V	filtrate volume, m^3.
v	velocity, m/s.
X	particle size, m.
X_0	characteristic particle size, m.
Y	cumulative fraction by weight less than size X, –.

Subscripts

0	initial.
A	attraction.
D	diffusion.
f	fibre.
G	gravity.
I	interception.
i	axis.
p	particle.
Pe	Peclet.
R	relative size group.
t	total.
vdW	van der Walls.
w	water.

approach that can consider the transport and entrapment of particles and its effect on the fluid dynamics and vice versa could be an important approach to understand the filtration process and aid in suggesting improvements.

The physical mechanisms involved in removal of particles from solutions via filtration processes can be considered at microscale using fundamental mathematical and kinetic models and at macroscale by observational (phenomenological) models. The former considers the complex structure of a filter medium and particles in their actual form, while in the latter, the medium is defined by its physical attributes (permeability, porosity and possibly pore size distribution) [5,6]. However, accurate models have not been developed for cartridge filters despite the importance of prediction of filtration performance in industry [7].

Adin and Rebhun [8] developed a model based on the material balance for an infinitesimal element of a filter bed. They assumed a constant diffusion coefficient and porosity, and therefore used a simplified mass transfer equation (Eq. (1)).

$$\frac{\partial C}{\partial x} + \frac{\partial \sigma}{\partial V} = 0 \tag{1}$$

where x is the filter depth, C the suspension concentration, σ the specific deposition and V the filtrate volume.

Eq. (1) was solved together with a kinetic equation (Eq. (2)) for the accumulation and detachment of particles,

$$\frac{\partial \sigma}{\partial V} = k_1 C(F - \sigma) - k_2 \frac{\sigma}{K} \tag{2}$$

where k_1 and k_2 are the accumulation and detachment coefficients, F the filter capacity and K the hydraulic permeability coefficient.

Many macroscopic models in literature are also based on the same approach, for example Han et al. [9] developed a model where the particle accumulation rate was based on a fundamental approach estimating the removal efficiency of a single collector. Similarly, Gitis et al. [10] provided a model for a full filtration cycle of a sand filter, assuming a uniform velocity and distribution of particles across the filter cross-section. However, in these models the effect of fluid dynamics and particle size distribution was ignored. Mays and Hunt [11] demonstrated that both particle deposition and deposit morphology depend on the fluid flow fields and the characteristics of the particles (e.g. diameter and density) and the porous media (e.g. porosity and collector diameter). Consequently, the models described above are only useful as long as the filter structure and operating conditions under investigation do not deviate from the model parameters. This would not be true for HWT systems incorporating cartridge filters, and as such there is a gap in knowledge around this important topic.

Therefore, a more general approach is needed to ensure flexibility in modelling of the cartridge filtration process, while considering the geometry of the unit. Computational fluid dynamics (CFD) is a powerful tool in this regard, allowing evaluation of flow properties at locations in a filtration unit that are not possible with lab based measuring instruments [12,13]. The large volume of data generated as a result of numerical CFD solutions can be visualised by vectors and contours [14], which has aided understanding to processes such as sedimentation [15]. Moreover, the data generated can be used to develop deep learning models to lower the computational time/costs of the simulations [16].

The application of CFD for simulation of filtration technologies has been widely applied, however few reports focus on HWT systems [17]. Subrenat et al. [18] investigated the pressure drop inside a cartridge housing with an activated carbon pleated filter for removal of volatile organic carbon compounds using a combination of 3D numerical

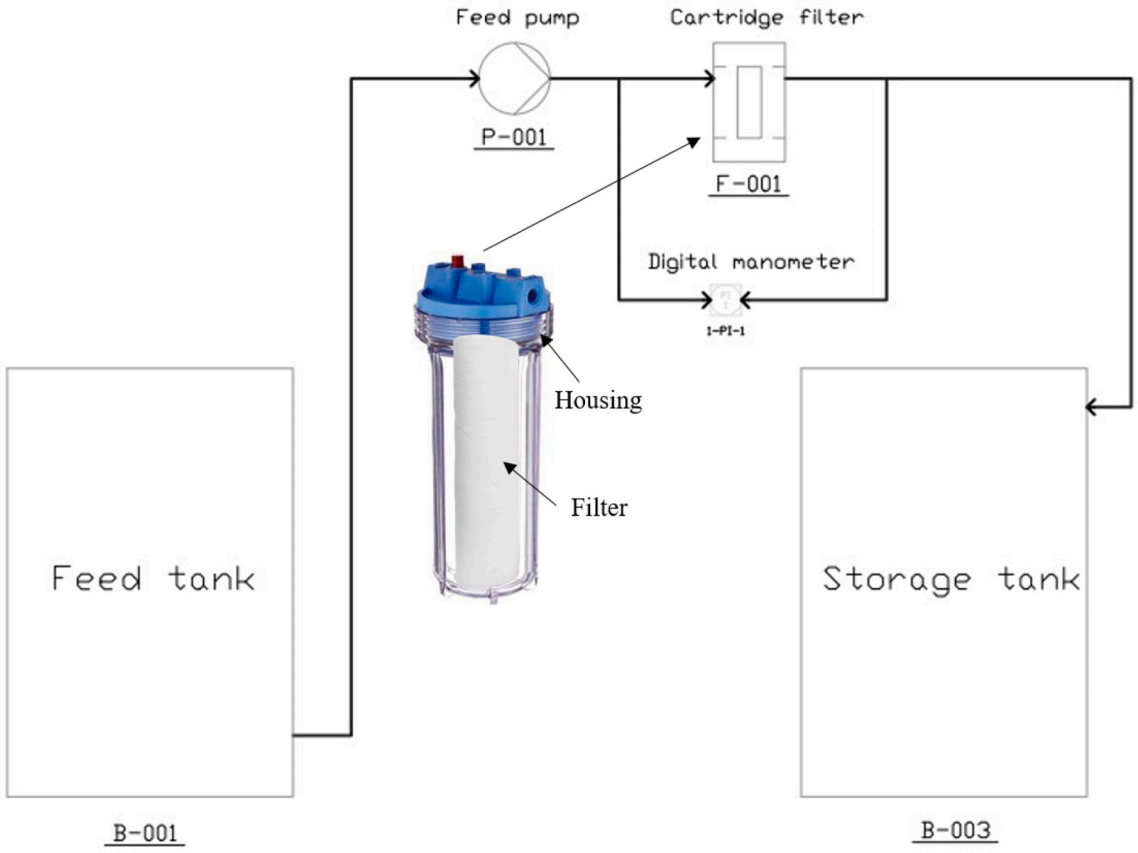

Fig. 1. The process flow diagram (PFD) of the filtration system and 10 in. cartridge filter element and housing used for the experiments.

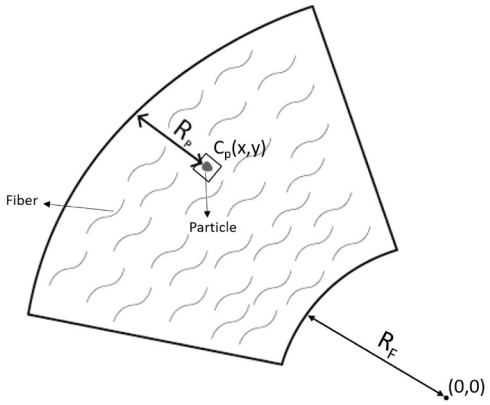

Fig. 2. Location of a particle in the porous zone, obtained by determining the coordinates of the cell (C_p) it is currently located in.

simulation and experimentation, to optimise pleat number for the filter element thereby minimising the pressure drop. Similarly, pressure drop and adsorption capacity of an activated carbon filter installed in an indoor air purifier was modelled by Roegiers and Denys [19], showing the spatial variation of adsorbed acetaldehyde at different time intervals.

Saalbach and Hunze [20] applied CFD to simulate the flow fields within membrane bioreactor (MBR) tanks for both hollow fibre and sheet membrane modules. The MBR plant was modelled at macro-scale level by considering membrane modules as porous media. Their work provided an approach to simulate large scale treatment systems that can be applied to other water and wastewater treatment plants.

Simulation of air/oil separation by cartridge filters was carried out by Basha [21], in which the flow fields and droplet trajectory were obtained. The Lagrangian approach was adopted for oil droplets while the Eulerian approach was used for the fluid flow. As oil droplets deposited over time, a decline in permeability was addressed by updating the inertial and viscous resistances in every cell of the porous zone.

Liu et al. [22] simulated dust removal by four ceramic filters, which were modelled as porous media in a housing. The number of deposited particles was summed to give the deposition mass in each cell and the pressure drop subsequently calculated by an empirical formula. The approach helped to explain experimental observations of non-uniform deposition of particles on the surface of the filter element.

Previous CFD studies have not investigated particle removal by cartridge filters commonly used for HWT; however, as described above, best practice was established through the Eulerian approach for the simulation of fluid flow and the Lagrangian approach for solid particles. This research builds on our previous work [23] in which it was observed that particles do not deposit homogeneously, but initially deposit in the lower and middle regions of the filter, as such the implementation of a novel CFD model adds to fundamental knowledge of particle deposition and through validation could be used in further design improvement to HWT systems.

2. Experimental materials and methods

Physical analysis of the filter materials and particles was required to inform and develop the parameters of the model and for experimental validation.

2.1. Instrumentation

A particle size analyser (Mastersizer 2000, Malvern Panalytical) was used to determine the size distribution of particles, with a scanning

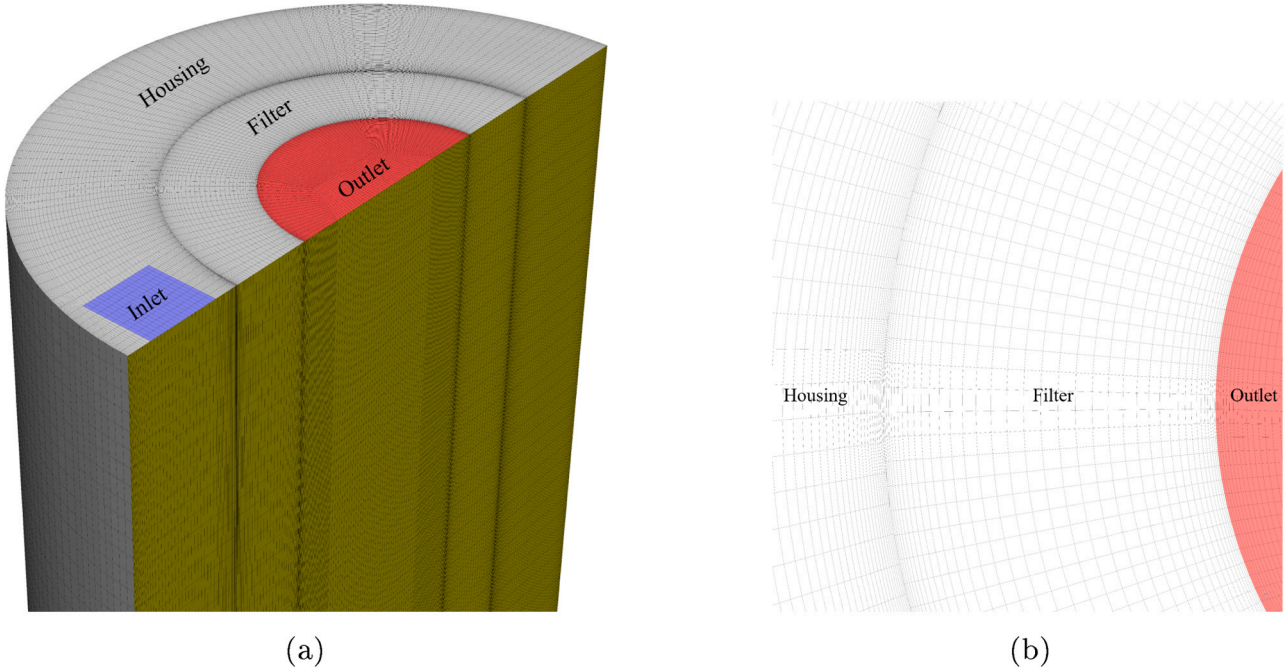

Fig. 3. (a) The computational mesh used in this study, showing the filter inlet (blue), the outlet (red), the axis of symmetry (green) and the wall surface (grey); (b) the top surface of the domain, showing the mesh refinement near the filter outer and inner surfaces.

electron microscope (JSM-6010, JEOL) used to determine the shape of particles and the internal structure of the fibrous filter. Prior to SEM imaging, samples were gold coated using a sputter coater (K500X, Emitech). Post-acquisition image analysis was undertaken using ImageJ software [24].

The pressure drop of the filter was measured using a digital manometer (2028P7, Digitron). A portable turbidity meter (HI-93703, Hanna Instruments) was used to measure the turbidity of water samples before and after filtration as a surrogate measurement for particle removal.

2.2. Materials

The filtration unit consisted of a standard 10 in. polypropylene spun filter element (Filter Logic, UK) and a filter housing (Finerfilters, UK) commonly used in small water treatment systems (Fig. 1). A commercial grade of diatomite, Standard Super-Cel® (Alfa Aesar, UK) with a density of 2300 kg/m^3 was added to water to represent polydisperse particles in turbid waters.

2.3. Experimental set-up and procedure

Two separate tanks were used to store the test water (feed tank) and the filtrate (storage tank). To prepare the test water, 3 g of Super-Cel was added to 25 L of tap water (Belfast, UK), making a 0.12 g/L suspension. The filter was placed inside the housing and the assembly filled with water (the computational domain was also filled with water at the start). The feed pump (Model 2095–204–412, Shurflo), pipes, fittings and digital manometer were connected as shown in the process flow diagram of the system (Fig. 1). Subsequently, the feed pump (fixed flow rate of 5 L/min) was turned on to pass the suspension through the filter. Trials were performed in triplicate, with pressure drop and turbidity measured every 2.5 L (the last 5 L in the tank was not processed).

3. Numerical methods

3.1. Particle size distribution function and shape

In order to represent the size of particles for modelling purposes, the Rosin-Rammler distribution function [25] was used; expressed as

$$Y = 1 - e^{\left[-\left(\frac{X}{X_0}\right)^n\right]} \tag{3}$$

where Y is the cumulative fraction by weight less than size X, n the 'uniformity constant' or 'spread parameter' describing the particles' uniformity, and X_0 the 'characteristic particle size', the size that 63.2% of particles were smaller than.

For non-spherical particles, shape can be quantified using the Wadell's sphericity (Ψ) [26], expressed as

$$\Psi = \frac{\text{surface area of a sphere with equal volume as the particle}}{\text{surface area of the particle}} \tag{4}$$

where Ψ is unitless and its value fractional.

3.2. Flow regime

In packed bed applications, Reynolds number is calculated as particle (fibre) Reynolds number (Re_f) via

$$Re_f = \frac{\rho v d_f}{\mu} \tag{5}$$

where v is superficial velocity, ρ density, μ dynamic viscosity, and d_f fibre equivalent diameter.

The flow regime was initially assumed to be laminar within the filter, while turbulent outside of the filter medium given water entered the housing via a 10 mm I.D. pipe. For turbulent flow regimes outside the filter, Reynolds-averaged Navier-Stokes (RANS) equations were used. Whilst based on laminar flow equations, the RANS include an additional turbulent viscosity in the terms for diffusion and non-pressure gradients of the momentum equation. There are several turbulence models, with

Fig. 4. Flow chart of the calculations implemented in this study.

k-ϵ being the most common in engineering applications [14]. Liu et al. [27] reported that for ceramic filters, pressure drop was predicted more accurately with k-ϵ than k-ω model and RSM (Reynolds stress model) and was therefore used in this study.

For turbulent flows, a wall function is used to approximate the drag at the wall and obtain the transition from zero velocity at the wall with no-slip boundary condition to the free stream turbulent core. Scalable wall functions were used due to the value of Y-plus ($y^+ > 11.225$), obtained from preliminary calculations.

3.3. Porous media model

The filter was considered as a homogeneous porous medium and included in the model as a computational zone with an additional momentum source term (S_i), including the viscous and inertial resistances as shown in Eq. (6).

$$S_i = -\left(\frac{\mu}{\alpha}v_i + C_2\frac{1}{2}\rho\left|v\right|v_i\right) \tag{6}$$

where $1/\alpha$ is permeability, C_2 the inertial resistance factor and v_i velocity in i direction—α and C_2 should be determined empirically [28].

The permeability ($1/\alpha$) was determined by running clean water through a clean cartridge filter, measuring the pressure drop and applying Darcy's law. The inertial resistance term was considered negligible as the relationship between flow rate and pressure drop was linear, due to the relatively small flow velocity.

Average fibre diameter was measured via analysis of the SEM images and where required in a model, a random number was generated within the 90th percentile of the measured fibres.

3.4. Particle deposition model

In order to include particle deposition, numerical models for removal

Table 1
Simulation settings.

Parameters	Value
Computational domain	
Domain size $i \times j \times k$ (m)	$0.045 \times 0.25 \times 0.045$
Mesh cells (millions)	1.2, 3.6, 4.8
Fluid phase	
Fluid density, ρ_w (kg/m^3)	998.2
Viscous model	Realizable k-ϵ
Fluid viscosity, μ_g (Pa · s)	0.001003
Inlet flow velocity (m/s)	0.3946
Fluid update time-step (s)	0.01
Particle phase	
Particle density, ρ_p (kg/m^3)	2300
Particle-wall restitution coefficient	$e_n = 0.75$, $e_t = 0.75$
No. of injection parcels (parcels/s)	2000
Drag force coefficient	Levenspiel and Haider[33]
Turbulent dispersion time scale constant, T_L	0.05
Particle update time-step (s)	0.01
New particle injection interval (s)	0.01

Table 2
User Defined Functions (UDFs) included in the simulations.

UDF	Function
UDF1	Initialize the UDMs for local porosity and permeability.
UDF2	Include the deposition and detachment models.
UDF3	Determine whether a particle deposits on the bottom wall or rebounds.

efficiency were needed. In this work, the fundamental model proposed by Tufenkji and Elimelech [29] was adopted, which provided equations for predicting single-collector (e.g. fiber) removal efficiency. In this model, the overall removal efficiency was the sum of the removal efficiency of different transport mechanisms—interception, gravitational sedimentation and Brownian diffusion. Eqs. (7–17) [5] were used to estimate the overall efficiency for each particle.

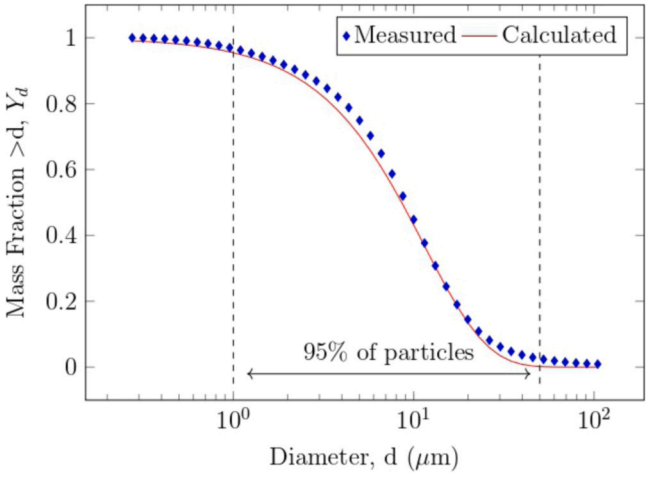

Fig. 6. The measured PSD for Standard Super-Cel® showing high correlation to that calculated by the Rosin-Rammler distribution function. The particle size range of 1–50 μm accounts for 95% of particles.

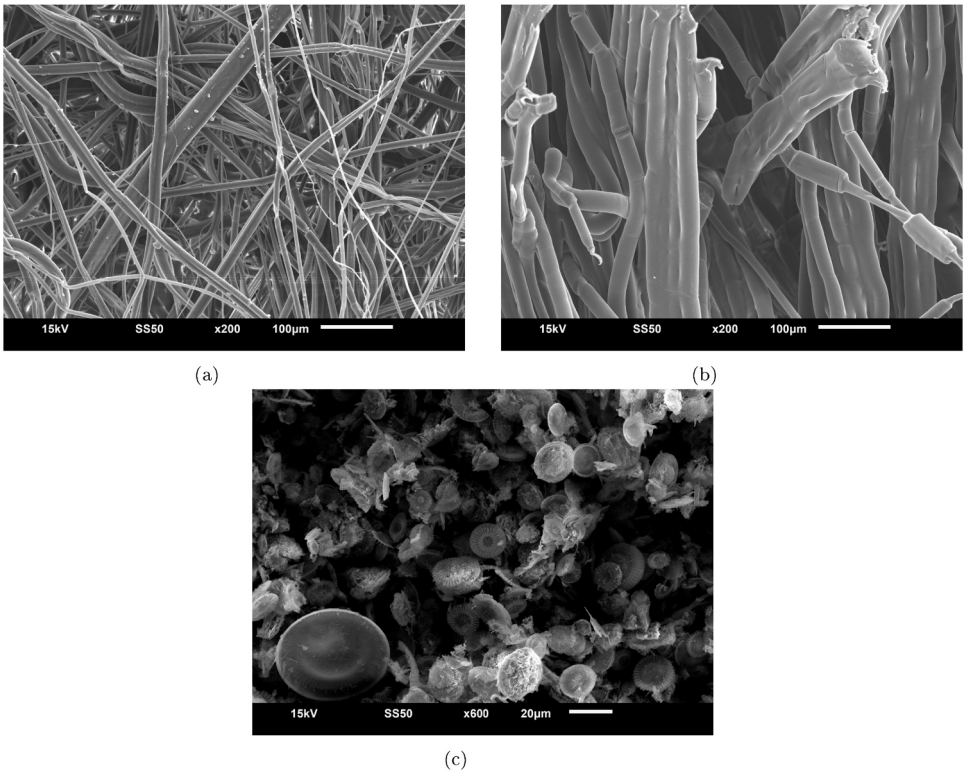

Fig. 5. SEM images of (a) the filter medium, (b) a slice of the filter placed vertically to measure the number of fibres in 1 mm, and (c) Standard Super-Cel® particles.

Table 3
Experimental results needed for the simulations.

Parameters	Value
Super-Cel particles	
Characteristic particle size, X_0 (μm)	11.48
Spread parameter, n	1.26
Particle sphericity	0.66
Porous media	
Filter cut-off size (μm)	90
Mean fibre diameter, d_f (μm)	25
Fibre diameter range, d_f (μm)	14.57–34.3
Filter porosity, ϵ	0.78
Filter initial permeability, α_0 (m^2)	11.5×10^{-12}
Eq. (24) constant, D ($1/m^5$)	1.49×10^{17}

$$N_R = \frac{d_p}{d_f} \tag{7}$$

$$N_G = \frac{g(\rho_p - \rho_w)d_p^2}{18\mu v_p} \tag{8}$$

$$N_{Pe} = \frac{3\pi\mu d_p d_f v_p}{k_B T} \tag{9}$$

$$N_{vdW} = \frac{H}{k_B T} \tag{10}$$

$$N_A = \frac{N_{vdW}}{N_R N_{Pe}} \tag{11}$$

$$\gamma = (1-\varepsilon)^{1/3} \tag{12}$$

$$A_S = \frac{2(1-\gamma^5)}{2-3\gamma+3\gamma^5-2\gamma^6} \tag{13}$$

$$\eta_I = 0.55 A_S N_A^{0.125} N_R^{1.675} \tag{14}$$

$$\eta_G = 0.22 N_R^{-0.24} N_{\mathrm{vdW}}^{0.053} N_G^{1.11} \tag{15}$$

$$\eta_D = 2.4 A_S^{1/3} N_R^{-0.081} N_{vdW}^{0.052} N_{Pe}^{-0.715} \tag{16}$$

$$\eta_t = \eta_I + \eta_G + \eta_D \tag{17}$$

1. A_S = porosity function, –
2. d_p = particle diameter, m
3. d_f = fibre diameter, m
4. k_B = Boltzmann constant, 1.381×10^{-23} J/K
5. T = absolute temperature, K
6. v_p = particle velocity, m/s
7. v_S = Stokes settling velocity, m/s
8. ε = bed porosity, –
9. γ = porosity coefficient, –
10. ρ_p = particle density, kg/m^3
11. ρ_w = liquid density, kg/m^3
12. μ = liquid viscosity, kg/(m s)
13. N_R = relative size group, –
14. N_G = gravity number, –
15. N_A = attraction number, –
16. N_{vow} = van der Walls number, –
17. N_{Pe} = Peclet number, –
18. D_L = diffusion coefficient, m^2/s
19. H = Hamaker constant, 1×10^{-29} J
20. η_I = transport efficiency due to interception, –
21. η_G = transport efficiency due to gravity, –
22. η_D = transport efficiency due to diffusion, –
23. η_t = total transport efficiency, –

$1/\eta_t$ represents the number of possible collisions with fibres required so that one real collision can be registered. Therefore, in order to determine whether a particle was deposited or not, $1/\eta_t$ was compared to the number of fibres that a particle has passed based on its location (Fig. 2), obtained by multiplying the distance of the particle from the outer surface of the filter (R_p) by the number of fibres per mm (n_f), estimated from SEM images (filter slices were imaged vertically). Any deposited particle was added to the number of collectors for the respective cell. This calculation was performed for every particle that reached the filter zone.

1. Possible collisions $= n_f \times 1000 \times R_p$
2. $R_p = \sqrt{x_{C_p}^2 + y_{C_p}^2} - R_F$
3. R_p = particle distance from the outer surface of the filter, m
4. R_F = the inner radius of the filter, m
5. n_f = approximate number of fibres in 1 mm

3.5. Filter cut-off size

In the deposition model explained above [29], the straining mechanism was not considered, whereas in this study some particles are larger than the pores of the filter. Therefore, based on several SEM images of the filter, a cut-off size was estimated (90 μ m).

3.6. Particle detachment model

A depositing particle might slide on the fibre because of the tangential drag force acting on it, resulting on its detachment. Bai and Tien [30] have proposed a model to determine whether a particle detaches, in which the magnitude of the net force between the tangential force and the friction force in the opposite direction is calculated, through Eqs. (18–22).

$$F_f = k_f \times \frac{H d_p}{12\delta^2} \tag{18}$$

$$k_f = k_f' S \tag{19}$$

$$S = \frac{6(1-\epsilon_0)}{d_f} \tag{20}$$

$$F_S = 2.551 \times 3\pi\mu \frac{A_S}{d_f} d_p^2 \frac{v_p}{\epsilon_0 - \sigma} \tag{21}$$

$$F = F_f - F_S \tag{22}$$

1. F_f = friction force against particle sliding, N
2. k_f = coefficient of sliding friction, –
3. δ = the separation distance between the particle and the fibre plane, 3×10^{-10} m
4. k_f' = proportionality constant, 3.79×10^{-6} m
5. S = specific surface area, m^{-1}
6. F_s = hydrodynamic drag force on a particle, N
7. F = net force acting on an depositing particle along the tangential direction, N

A particle slips when F is a negative value, i.e. the tangential drag force is dominant over the friction force.

3.7. Local permeability

As the simulations were transient, an equation that related local permeability to the deposited particles in mesh cells at every time step was needed. Local porosity at time t (ϵ_{c_t}) was given by Eq. (23).

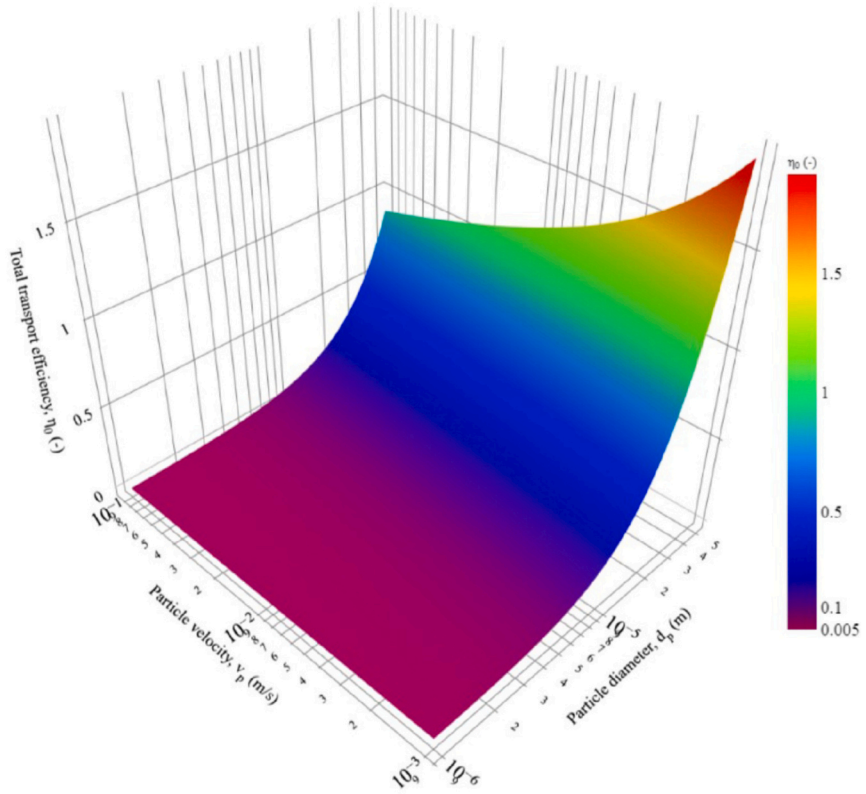

(a)

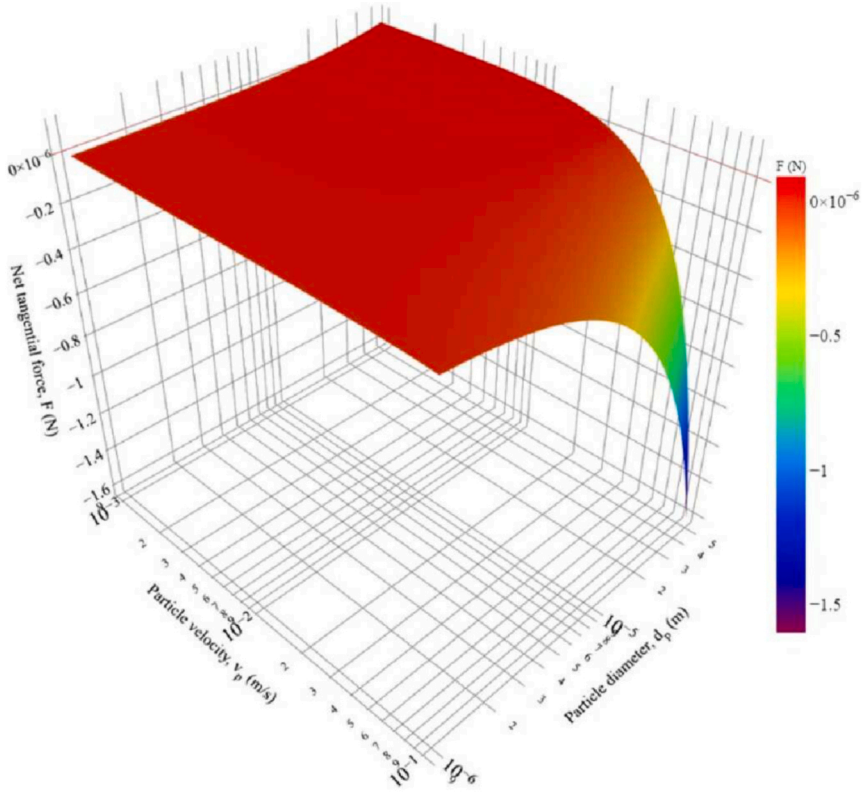

(b)

Fig. 7. (a) η_t versus particle size and velocity. (b) Net tangential force (F) versus particle size and velocity. ($d_f = 25\ \mu m$, T = 288.15 K, $\epsilon_0 = 0.78$, $\rho_w = 998\ kg/m^3$, $\rho_p = 2300\ kg/m^3$, $k_f = 3.79 \times 10^{-6}$, $\delta = 3 \times 10^{-10}$ m).

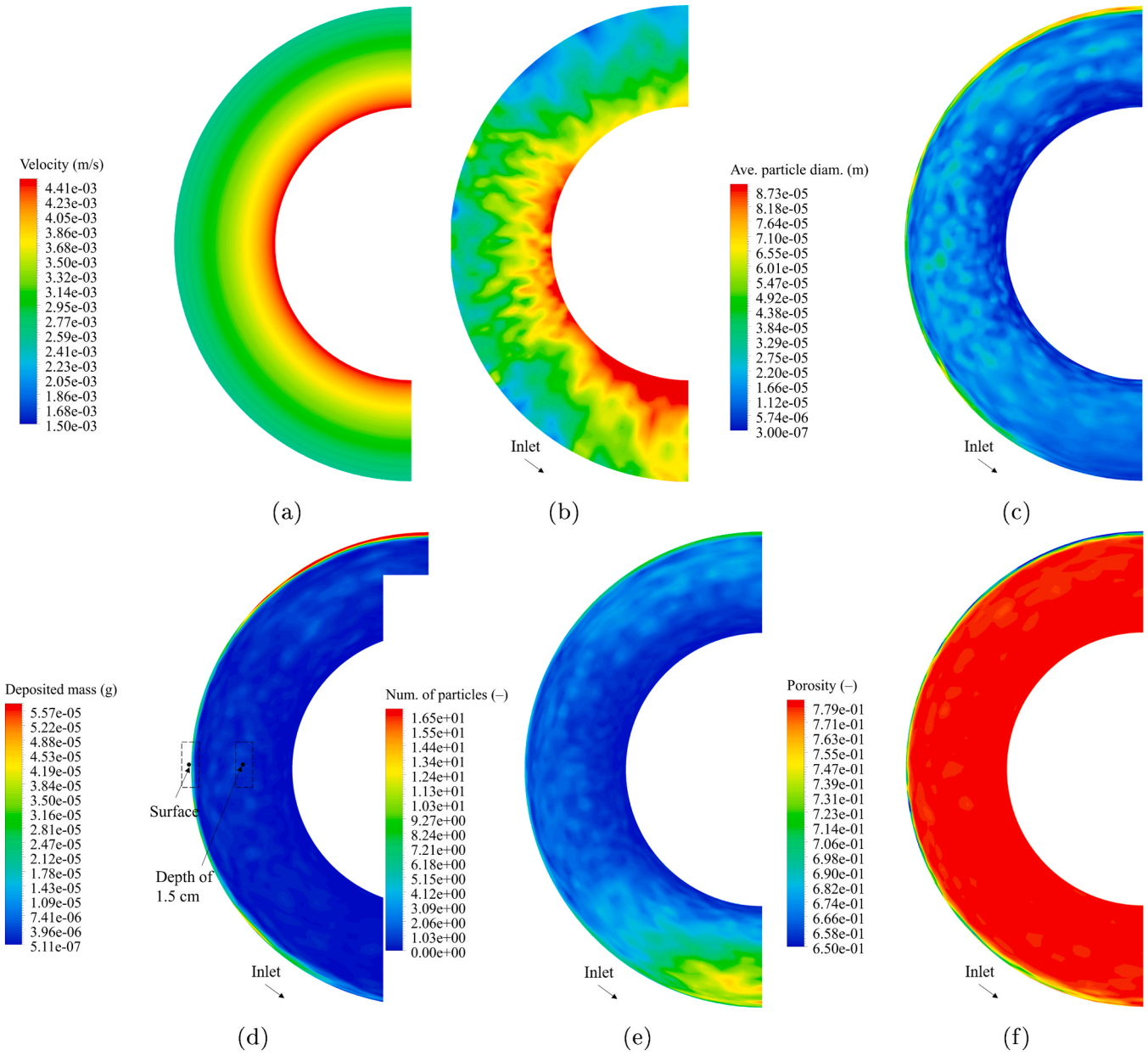

Fig. 8. Velocity contours on a plane (a cross sectional slice) at the middle (12.5 cm from the top) of the filter (a) at the start (clean) and (b) end of the simulation (2.4 g Super-Cel processed). Contours of (c) average diameter, (d) mass, and (e) number of deposited particles as well as (f) local porosity at the middle of the filter (12.5 cm from the top) after processing 2.4 g Super-Cel.

$$\epsilon_{c_t} = \epsilon_{c_{t-1}} - \frac{V_{p_t}}{V_{c_t}} \tag{23}$$

where V_{c_t} and V_{p_t} are the volume of the cell and the deposited particle(s) at time t, respectively.

An equation was written for local resistance based on the Kozeny-Carman equation and Darcy's law,

$$\alpha_{c_t} = \alpha_{c_{t-1}} + \sum_{t=0}^{t} \left(\frac{D \cdot V_{p_t}}{\epsilon_{c_t}^2}\right) \tag{24}$$

where D is an empirical constant, obtained by performing preliminary trials with multiple commercial cartridge filters and Super-Cel particles.

Therefore, at every time step, the volume of the deposited parcels is multiplied by an empirical constant, divided by the square of the porosity and added to the local resistance in the previous time step stored in a User Defined Memory (UDM) for the respective mesh cell.

Complete filling of a cell volume with particles was not considered as the amount of particles in the experiment was relatively small relative to the filter's volume.

3.8. Particle motion

The Lagrangian framework was adopted for the motion of particles. The trajectory of particles was predicted by integrating the force balance acting on the particles, written as

$$m_p \frac{d\vec{u}_p}{dt} = m_p \frac{\vec{u} - \vec{u}_p}{\tau_r} + m_p \frac{\vec{g}(\rho_p - \rho)}{\rho_p} + \vec{F} \tag{25}$$

where m_p, u_p, ρ_p and τ_r are particle mass, velocity, density and relaxation time, respectively [31].

The first term on the right side is the drag force, which is a function of the particle relaxation time (τ_r), the time required for a particle to adjust

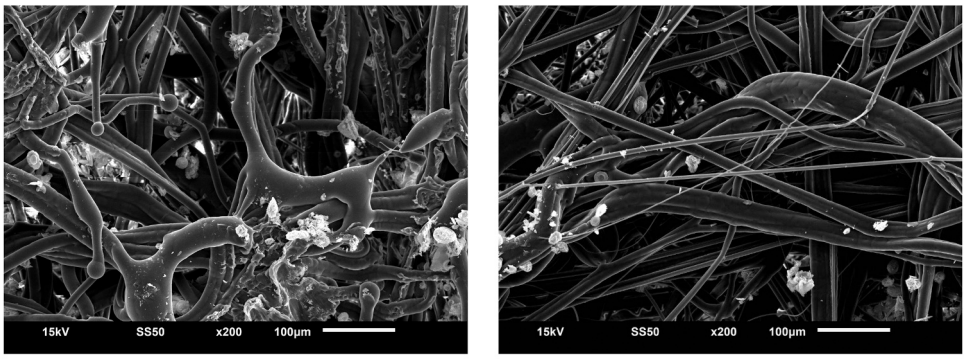

Fig. 9. SEM images of two slices of the filter taken from the middle (12.5 cm from the top) of the filter after processing 2.4 g Super-Cel. A slice taken from (a) the surface and (b) the depth of 1.5 cm (approximate locations shown in Fig. 8d).

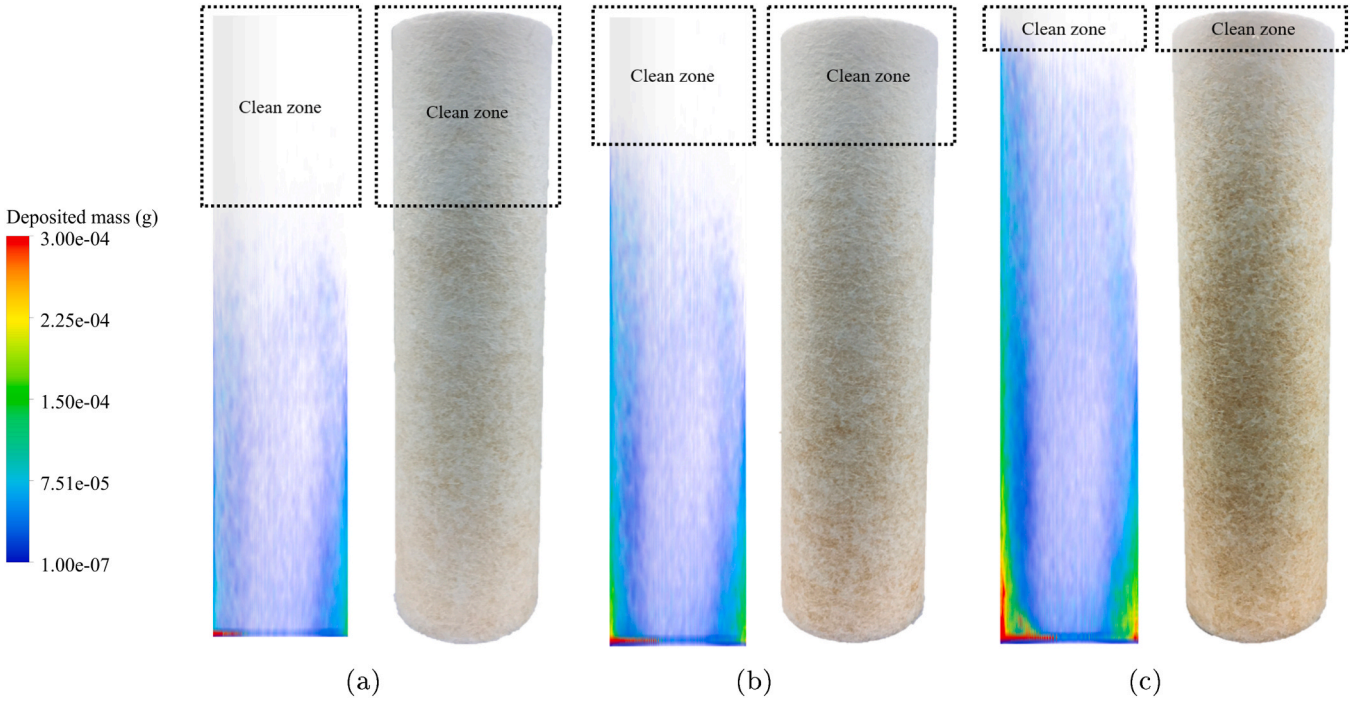

Fig. 10. Deposition of particles on the filter (real and simulation side by side). After (a) 0.6 g, (b) 1.2 g and (c) 2.4 g was processed. (Due to the transparency of the contour in the simulation results, deposition in the depth is also visible but cannot be observed in the images of the experimental filters.).

its velocity, expressed as

$$\tau_r = \frac{\rho_p d_p^2}{18\mu}\frac{24}{C_D Re} \tag{26}$$

where Re is the relative Reynolds number [32]. The drag coefficient, C_D, used for non-spherical particles can be expressed as,

$$C_D = \frac{24}{Re}\left[1 + e^{(2.3288-6.4581\psi+2.4486\psi^2)}Re^{(0.0964+0.5665\psi)}\right] + \frac{Re \times e^{(4.905-13.8944\psi+18.4222\psi^2-10.2599\psi^3)}}{Re + e^{(1.4681+12.2584\psi-20.7322\psi^2+15.8855\psi^3)}} \tag{27}$$

where ψ is Wadell's sphericity [33].

Turbulent dispersion was also considered in particle motion. When particles are not located near a wall, turbulence dispersion dominates over gravity and Brownian motion [34]. Using the built-in stochastic tracking model in Ansys Fluent software, the dispersion of particles can be predicted by making use of the integral time scale, T_L, which is proportional to the particle dispersion rate. For small particles which move with the fluid, the integral time scale can be approximated as,

$$T_L = C_L\frac{k}{\varepsilon} \tag{28}$$

where T_L and C_L are the fluid Lagrangian integral time and time scale constant, respectively.

Other forces such as lift, Brownian and virtual mass have not been considered due to their negligible effect.

In simulations where the volume fraction of particles is small, one way coupling (particles to the fluid flow) is deemed sufficient [35], which has been implemented in this work. As it was prohibitive to track the same number of particles as in the real experiment, in the simulations, a number of 'parcels' were tracked instead - 2000 parcels were injected every time step (0.01 s). Each parcel represented a fraction of the total mass flow rate released in a time step with a specified particle diameter and a relaxation time appropriate for a single particle [31].

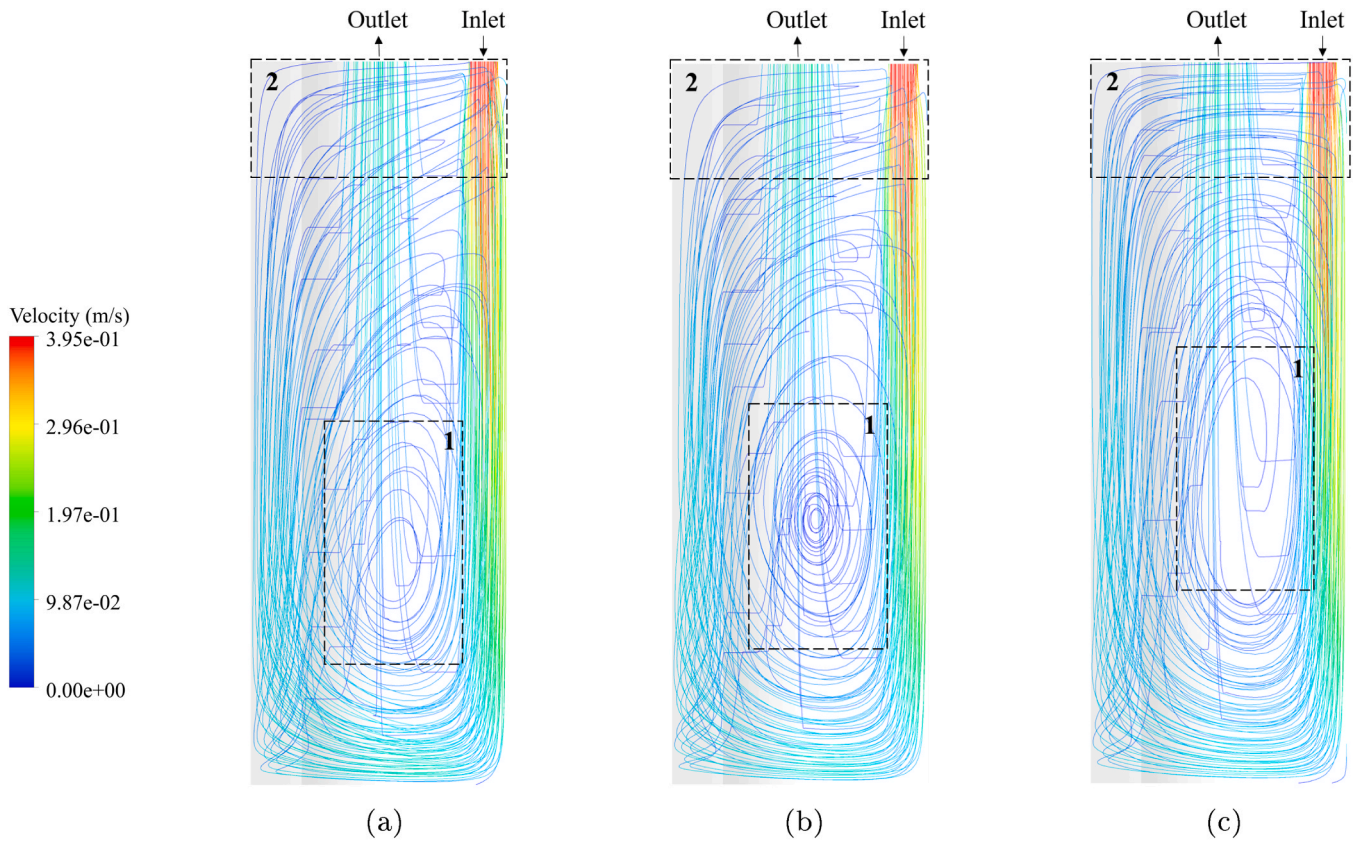

Fig. 11. The fluid streamlines alter due to the deposition of particles and change in the local permeability. After (a) 0.6 g, (b) 1.2 g and (c) 2.4 g was processed.

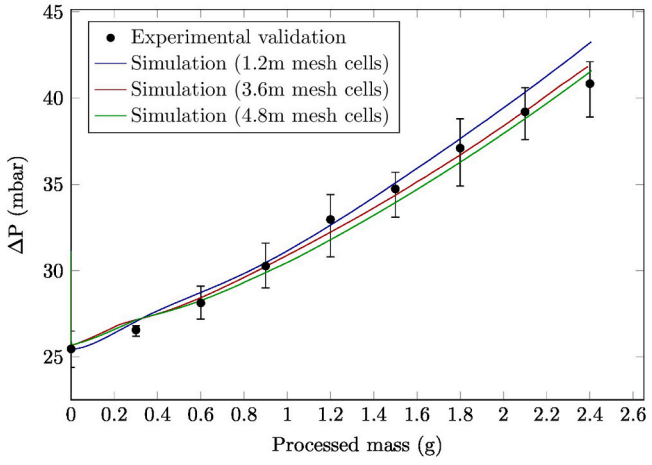

Fig. 12. ΔP against the processed mass for both the experiment and the simulation.

3.9. Particle-wall collisions

Particle rebound following collision with a wall was calculated by the default model within Ansys Fluent [31] based on the work of Wakeman and Tabakoff [36], which calculates the rebound velocity by considering the coefficient of restitution (e):

$$e_n = \frac{v_{2,n}}{v_{1,n}} \tag{29}$$

$$e_t = \frac{v_{2,t}}{v_{1,t}} \tag{30}$$

where v_n and v_t are the particle velocity normal and tangent to the wall, respectively, and the subscripts 1 and 2 refer to before and after collision, respectively.

The coefficient should be determined based on the material of the wall, which in the case of the filter housing, hard plastic, the restitution coefficient value was 0.75–0.8 [37].

In order to avoid particles re-circulating near the bottom of the housing, without limiting the number of time steps for trajectory calculation, an arbitrary small value was considered for the velocity of particles hitting the bottom wall (v_{crit} = 0.005 m/s) below which the mass of a particle was registered in a UDM and removed from the domain.

3.10. Computational mesh

The computational mesh for this study was created by Ansys ICEM CFD, shown in Fig. 3a, with ≈ 1.2 million high quality hexahedral mesh cells. As the cartridge filter was symmetrical, only half was considered in the model to reduce the required computational time. Mesh near the housing wall and the filter inner and outer surfaces was refined (Fig. 3b) by determining a first element thickness and an expansion factor (1.1) in order to capture the fields' gradients.

To evaluate the effect of mesh size on the pressure drop results, simulations with two smaller meshes—3.6 and 4.8 million mesh cells—were also performed. In Eq. (24), α_{c_t} defines the resistance for a cell; therefore, as mesh cells are divided, when a particle deposits, a smaller volume of the filter zone is affected. To counter this effect, the empirical parameter D was multiplied by the size ratio of the new mesh to the original mesh.

$$D' = D \times \frac{\text{No. of mesh cells in the current domain}}{\text{No. of mesh cells for which D (Eq. (24)) was obtained}} \tag{31}$$

3.11. Solution

The calculation sequence for the simulation is summarized in the flow chart shown in Fig. 4, and the simulation settings in Table 1. A commercial software (ANSYS Fluent) was used to solve the governing equations, and custom User Defined Functions (UDFs), summarised in Table 2, were developed in order to include the additional models/functions required. In the simulation, the SIMPLE scheme with double-precision accuracy, the first-order implicit scheme for temporal discretization, the second-order upwind scheme for momentum, and the PRESTO! scheme for pressure coupling were used. The time step in the simulations was 0.01 s for both the fluid and particle phase, and the simulations were stopped when 2.4 g of Super-Cel was processed (i.e. deposited within the filter, on the bottom wall or escaped from the outlet), which made the simulation computational time much shorter than the real experiment.

The computer used was equipped with two Intel® Xeon® Processor E5645 (12 CPU cores) and 48 GB of RAM.

3.12. Model validation

In order to validate the results obtained in the CFD simulations and demonstrate the accuracy of the modelling work, physical changes that could be experimentally measured were reported. The deposited particles on a cross section at the middle of the filter (12.5 cm from the top) after processing 2.4 g Super-Cel were visualised and compared with SEM images taken from slices removed from the outer surface at a depth of 1.5 cm (half of the distance between the outer and inner surfaces). The deposited particles within the volume of the filter were visualised and compared with digital photographs taken from the filter's surface using a camera. Lastly, the predicted pressure drop based on Eq. (24) and Eq. (31) was reported for three mesh sizes (1.2 m, 3.6 m and 4.8 m) and compared with the pressure drop measured during the experimental validation.

4. Results and discussion

To inform model development, physical analysis of the filter materials and particles was undertaken.

4.1. Filter, particle and flow characterisation

SEM images of the filter element (e.g. Fig. 5a) showed the filter to comprise of randomly oriented fibres, with diameter sizes varying from 1.1 to 34.3 μm; 90% were between 14.57 and 34.3 μm, with the mean fibre diameter (d_c) being 25 μm. The number of fibres per mm (n_f), obtained by SEM imaging (e.g. Fig. 5b), was 44 per mm. The cut-off size of the filter was determined to be 90 μm. The porosity (ϵ) of the filter was estimated to be 0.78 based on the density of polypropylene fibres, 0.9 g/cm^3 [12], and the measured volume and weight of the filter.

The Reynolds number within the filter was calculated to be 0.044 by considering the mean fibre diameter (25 μm) and the superficial velocity (0.00196 m/s) - pump flow rate was 5 L/min and the surface area of the filter 0.0424 m^2. In Eq. (5), due to the exclusion of properties such as surface roughness, Reynolds number for transition between laminar and turbulent flow was empirical based give the flow regime: laminar ($Re_f <$ 10), transitional ($10 < Re_f < 300$) or turbulent ($Re_f > 300$) [38].

By fitting the PSD data obtained for Standard Super-Cel® to the Rosin-Rammler distribution function (Eq. (3)), the characteristic particle size and the spread parameter were determined to be 11.48 μm and 1.26, respectively. The measured and calculated PSD values (Fig. 6) showed good agreement with an R-squared (R^2) of 0.994. Given Super-Cel® particles were observed to be mostly disk shaped (Fig. 5c), the sphericity value for a thin disk can be assumed to be 0.66 [39].

The average permeability of the filter, estimated empirically to be 11.5×10^{-12} m^2, which assumed to be isotropic; the empirical constant (D) in Eq. (24) was determined to be 1.49×10^{17} 1/m^5. A summary of the experimental results obtained for the simulations is provided in Table 3.

4.2. Particle deposition and detachment

In order to establish the relationship between particle deposition and particle size/velocity (Eqs. (7)–(17)), the total transport efficiency (η_t) versus particle size and filtration velocity for a clean filter, based on a particle size and a velocity range of 1–50 μm and 0.001–0.1 m/s, respectively, is plotted in Fig. 7a, where $\eta_t > 1$ dictates that the particle will likely deposit on the first fibre that it encounters. For the mean fibre diameter of 25 μm, particle diameters above 32.6–49.7 μm had an η_t of > 1 in the the velocity range of 0.001–0.0325 m/s, respectively. The velocity of a particle is inversely related to η_t; therefore, the likelihood of deposition increases as a particle loses momentum within the porous medium.

In order for a particle to be registered as deposited, the tangential drag force should not be larger than the friction force in the opposite direction, which is influenced by particle size, fibre size and pressure gradient as a result of local deposition. Fig. 7b shows the results for the net tangential force (Eqs. (18)–(22)) for a clean filter and the particle size and velocity range in the simulations. An F value below 0 implies a particle slips and will not be deposited. The net force has an inverse relationship with both particle size and velocity and through comparison of the results for the attachment and detachment models, it can be concluded that as the velocity of a small particle decreases, it is more likely for the particle to attach without slipping, while a particle of larger size leads to increased probability of both deposition and slippage. Therefore, particle size alone cannot be a sole determinant of particle deposition, with a requirement for the consideration of local velocity.

4.3. Cross section velocity gradient and particle deposition

Modelling confirmed the velocity of the fluid changed within the cartridge filter both horizontally and vertically due to the cylindrical geometry (e.g. Fig. 8a). The velocity gradient could be also impacted upon by particle deposition (e.g. Fig. 8b), leading to dispersed deposition of particles between the inner and outer surfaces (Fig. 8c).

Figure 8c shows the contour of deposited particles' average diameter at 12.5 cm from the top (middle of the filter) at the end of the simulation (after processing 2.4 g Super-Cel), demonstrating the penetration of particles as a result of particle size. Particles above 90 μm were removed close to the outer surface of the filter given the cut-off size included in the simulations. As $V_p \propto d_p^3$, deposition of large particles in small numbers resulted in a much higher mass (Fig. 8d) and consequently reduction in porosity (Fig. 8f) than fine particles in larger numbers (Fig. 8e).

To validate the model, SEM images of filters following processing of 2.4 g Super-Cel were examined. Fig. 9 shows images of cross sectional slices of the filter taken at the midway point of 12.5 cm, with a higher number of particles observed at the surface (Fig. 9a) than at a depth of 1.5 cm into the filter (Fig. 9b) - at the magnification of the images - confirming that a higher particle mass was likely to deposit on the outer region than within the filter.

4.4. Surface deposition and streamlines

Figure 10 shows the deposition of particles onto the surface of the filter attained through simulation in comparison to images of the filters taken from validation experiments, based on the mass of solids processed (i.e. total mass in the domain minus the mass floating in the housing). Particle deposition was observed to start in the lower and middle regions of the filter, and as the hydraulic resistance in these

regions increased, the flow path in the housing was altered, as shown in Fig. 11. The highlighted zones (dashed rectangles) point to the recirculation zone (number 1) and the density of streamlines at the upper region of the housing (number 2). As parcels deposit, the recirculation zone moved upward and, consequently, the flow field progressed towards the upper region of the filter, resulting in increased rates of particle deposition. Although water circulated in the housing, the streamlines in the filter were perpendicular to the Z direction (Fig. 11), however, once water passed through the porous zone, it moved upward towards the outlet with increased velocity given the lower resistance in the pipe network.

4.5. Pressure drop and particle removal efficiency

Fig. 12 shows the pressure drop (ΔP) obtained against the processed mass for both the simulations with different mesh sizes and validation experiments. Agreement can be observed between the results, with Root Mean Square Percentage Error (RMSPE) value being 2.46%, 1.49% and 1.95% for 1.2 m, 3.6 m and 4.8 m mesh cells, respectively. Regarding particle removal results, removal in the experiments was variable, but turbidity removal reached $>$ 90% after a short period. In the simulation, a total removal efficiency of 91.5%, of which 85% was due to filtration and 6.5% due to settling, was recorded during the simulation, showing agreement with the laboratory experiments.

5. Conclusion

This work explored the process both at micro- and macro-level to provide a complete understanding the underpinning filtration mechanisms. The process was simulated by considering the fluid dynamics and particle motion equations as well as models for particle deposition, detachment and rebound, and for the first time providing a comprehensive modelling methodology for cartridge filtration units.

This study showed that the larger particles were entrapped at the outer part of the filter, significantly reducing permeability. Hence, manufacturing multilayer filters with declining porosity from the outer to inner part can result in improved filter runs. Novel housing designs which promote particle settlement, e.g. a hydrocyclone, can remove large particles responsible for the loss in permeability at the outer surface; therefore, improving efficiency and filter lifetime. In addition, based on the PSD of particles in a specific water, customized filters can be designed by performing a CFD simulation and adjusting the filter thickness and porosity, developing new opportunities to improve filter efficiency and ultimately increase the usable lifetime of the filters - providing safe water at lower cost to users.

The simulation and experimental validation demonstrated agreement with respect to particle removal, pattern of particle deposition (i.e., particles first depositing on the lower and middle region of the filter and as the local pressure drop increased particles depositing in the upper region) and pressure drop (RMSPE = 1.49–2.46%). The method and approach developed in this study can be used as a powerful tool to test different filter designs and filter materials with minimal parameter adjustment, saving laboratory time and expense.

Moreover, this study provides a basis to improve the performance of cartridge filters aiming at longer filtration runs and, consequently, provide practical and economic benefits for the end users.

CRediT authorship contribution statement

Arsalan Afkhami: Conceptualization, Methodology, Software, Validation, Formal analysis, Investigation, Resources, Data Curation, Writing - Original Draft, Visualization. **Alan Brown**: Writing - Review & Editing. **Lyda P. Sabogal-Paz**: Writing - Review & Editing. **Dorian Dixon**: Writing - Review & Editing. **Nigel G. Ternan**: Writing - Review & Editing. **Patrick S. M. Dunlop**: Writing - Review & Editing, Supervision, Project administration, Funding acquisition.

Declaration of Competing Interest

The authors declare that they have no known competing financial interests or personal relationships that could have appeared to influence the work reported in this paper.

Data Availability

No data was used for the research described in the article.

Acknowledgements

This study is part of SAFEWATER projects supported by Global Challenges Research Fund (GCRF) and UK Research and Innovation (SAFEWATER; EPSRC Grant Reference EP/P032427/1). We also acknowledge support from Ulster University's VCRS Postgraduate Scholarship Scheme (AA).

Statement

The authors hereby declare previous originality check, no conflict of interest and open access to the repository of data used in this paper for scientific purposes.

References

[1] WHO/UNICEF, Drinking Water, Sanitation and Hygiene in Schools - Global baseline report 2018, 2018.
[2] WHO, WHO water, sanitation and hygiene strategy 2018–2025, 2018.
[3] WHO, Results of round II of the WHO international scheme to evaluate household water treatment technologies, 2019.
[4] WHO/UNICEF, Progress on drinking water, sanitation and hygiene: 2017 update and SDG baselines, 2017.
[5] J.C. Crittenden, R.R. Trussell, D.W. Hand, K.J. Howe, G. Tchobanoglous, MWHas Water Treatment, 2012.
[6] S. Osterroth, Mathematical models for the simulation of combined depth and cake filtration processes, Ph.D. thesis, University of Kaiserslautern, 2018.
[7] S.A. Hosseini, Modeling Particle Filtration and Caking In Fibrous Filter Media, Ph. D. thesis, Virginia Commonwealth University, 2011.
[8] A. Adin, M. Rebhun, Model to predict concentration and head-loss profiles in filtration, Am. Water Work. Assoc. 69 (1977) 444–453.
[9] S. Han, C.S.B. Fitzpatrick, A. Wetherill, Mathematical modelling of particle removal and head loss in rapid gravity filtration, Sep. Sci. Technol. 43 (2008) 1798–1812.
[10] V. Gitis, I. Rubinstein, M. Livshits, G. Ziskind, Deep-bed filtration model with multistage deposition kinetics, Chem. Eng. J. 163 (2010) 78–85.
[11] D.C. Mays, J.R. Hunt, Hydrodynamic aspects of particle clogging in porous media, Environ. Sci. Technol. 39 (2005) 577–584.
[12] I.M. Hutten, Handbook of Nonwoven Filter Media, Elsevier Ltd.,, 2016.
[13] A. Uppu, A. Chaudhuri, S.P. Das, N. Prakash, CFD modeling of gypsum scaling in cross-flow RO filters using moments of particle population balance, J. Environ. Chem. Eng. 8 (2020), 104151.
[14] J. Tu, G.-H. Yeoh, C. Liu, Computational Fluid Dynamics: A Practical Approach, 2018.
[15] R.W. Samstag, J.J. Ducoste, A. Griborio, I. Nopens, D.J. Batstone, J.D. Wicks, S. Saunders, E.A. Wicklein, G. Kenny, J. Laurent, CFD for wastewater treatment: An overview, Water Sci. Technol. 74 (2016) 549–563.
[16] A. Marcato, G. Boccardo, D. Marchisio, A computational workflow to study particle transport and filtration in porous media: Coupling CFD and deep learning, Chem. Eng. J. 417 (2021), 128936.
[17] L.Y.C.P. Hojo, R.V. d.P. Rezende, S.R. Lautenschlager, L.P. Sabogal-Paz, Household slow sand filters operating in continuous and intermittent flows: Computational fluid dynamics simulation and validation by tracer experiments, Chem. Eng. Sci. 247 (2022), 117058.
[18] A. Subrenat, J. Bellettre, P. LeCloirec, 3-D numerical simulations of flows in a cylindrical pleated filter packed with activated carbon rcloth, Chem. Eng. Sci. 58 (2003) 4965–4973.
[19] J. Roegiers, S. Denys, CFD-modelling of activated carbon fibers for indoor air purification, Chem. Eng. J. 365 (2019) 80–87.
[20] J. Saalbach, M. Hunze, Flow structures in MBR-tanks, Water Sci. Technol. 57 (2008) 699–705.
[21] N. Basha, FD study of filtration process in moulded filters within a vacuum pump, In: FILTECH 2016 Conf. Proc. 2016.
[22] K. Liu, Y. Zhao, L. Jia, R. Hao, D. Fu, A novel CFD-based method for predicting pressure drop and dust cake distribution of ceramic filter during filtration process at macro-scale, Powder Technol. 353 (2019) 27–40.
[23] A. Afkhami, M. Marotta, D. Dixon, N.G. Ternan, L.J. Montoya-Jaramillo, M. Hincapie, L. Galeano, P. Fernandez-Ibanez, P.S. Dunlop, Assessment of low-cost

cartridge filters for implementation in household drinking water treatment systems, J. Water Process Eng. 39 (2020), 101710.
[24] C.A. Schneider, W.S. Rasband, K.W. Eliceiri, NIH image to ImageJ: 25 years of image analysis, Nat. Methods 9 (2012) 671–675.
[25] P. Rosin, E. Rammler, Die Kornzusammensetzung des Mahlgutes im Lichte der Wahrscheinlichkeitslehre, Kolloid-Z. 67 (1934) 16–26.
[26] H. Wadell, Sphericity and roundness of rock particles, J. Geol. 41 (1933) 310–331.
[27] K. Liu, Y. Zhao, L. Jia, Simulation of dust deposition process in ceramic filter under different filtration modes by a novel CFD-based method, Sep. Purif. Technol. 233 (2020), 116039.
[28] ANSYS, ANSYS Fluent User's Guide, 2018.
[29] N. Tufenkji, M. Elimelech, Correlation equation for predicting single-collector efficiency in physicochemical filtration in saturated porous media, Environ. Sci. Technol. 38 (2004) 529–536.
[30] R. Bai, C. Tien, Particle detachment in deep bed filtration, J. Colloid Interface Sci. 186 (1997) 307–317.
[31] ANSYS ANSYS Fluent Theory Guide, 2018.
[32] A.D. Gosman, E. Ioannides, Aspects of computer simulation of liquid-fuelled combustors, J. Energy 7 (1983) 482–490.
[33] O. Levenspiel, A. Haider, Drag coefficient and terminal velocity of spherical and nonspherical particles, Powder Technol. 58 (1989) 63–70.
[34] A. Li, G. Ahmadi, Dispersion and deposition of spherical particles from point sources in a turbulent channel flow, Aerosol Sci. Technol. 16 (1992) 209–226.
[35] A.A. Mofakham, G. Ahmadi, On random walk models for simulation of particle-laden turbulent flows, Int. J. Multiph. Flow. 122 (2020), 103157.
[36] T. Wakeman, W. Tabakoff, Measured particle rebound characteristics useful for erosion prediction. (1982).
[37] M. Sommerfeld, N. Huber, Experimental analysis of modelling of particle-wall collisions, Int. J. Multiph. Flow. 25 (1999) 1457–1489.
[38] M.J. Baker, CFD simulation of flow through packed beds using the finite volume technique, Ph.D. thesis, 2011.
[39] R.P. Chhabra, L. Agarwal, N.K. Sinha, Drag on non-spherical particles: An evaluation of available methods, Powder Technol. 101 (1999) 288–295.